



An opinion on catalyst degradation mechanisms during catalyst support focused accelerated stress test (AST) for proton exchange membrane fuel cells (PEMFCs)

Raghunandan Sharma, Shuang Ma Andersen*

Department of Chemical Engineering, Biotechnology and Environmental Technology, University of Southern Denmark, Campusvej 55, DK-5230, Odense M, Denmark

ARTICLE INFO

Keywords:

Accelerated stress test (AST)
Support corrosion
Platinum nanoparticle
Ostwald ripening
Proton exchange membrane fuel cells (PEMFCs)

ABSTRACT

Accelerated stress test (AST) protocol meant to study the durability of catalyst support in a polymer electrolyte membrane fuel cell (PEMFC) electrode has been critically evaluated. For nanoparticulate catalysts supported on high surface area conductive materials (e.g. Pt/C), potential cycling meant to study the support durability causes significant impact on the catalyst particles presumed to be passivated due to formation of oxide layer. X-ray diffraction (XRD) patterns of pre-AST and post-AST samples suggest significant change in crystallite size during potential cycling between 1.0 and 1.6 V (vs. RHE), which may be considered to growth induced by dissolution/redeposition rather than particle growth through agglomeration due to support corrosion. Significant (~50%) electrochemical surface area loss due to catalyst particle growth during support corrosion AST should be taken into account while development/screening of durable catalyst supports. To reduce such contribution, frequent observation cycle should be minimized.

1. Introduction

Platinum group metal (PGM)-based electrocatalysts are of significant importance, especially for renewable electrochemical energy conversion devices [1,2] such as proton exchange membrane fuel cells (PEMFCs). Widely adopted in both industries and research installations, state-of-the-art electrodes in PEMFCs consist of Pt/Pt-alloy nanoparticles supported on high surface area carbon. Owing to their high initial cost, assessment and enhancement of the durability of such electrocatalysts has acquired considerable research interest [3–6]. The catalytic performance degradation mechanisms under PEMFC operating conditions may affect either the catalyst particle or the surrounding environment responsible for providing proton, electron and reactant accessibility to the catalyst particles. Moreover, while the former dominates under steady state conditions, support corrosion takes place mainly during startup/shutdown due to development of potentials ranging between 1.4 and 1.75 V [7–11]. Modifications of catalyst composition, surface structure, etc. may be used to mitigate the catalyst particle degradation, while highly durable catalyst support materials are being explored to minimize the later [4,12–14].

Development of durable catalyst support materials for PEMFC applications requires fast evaluation of durability through accelerated stress test (AST) under predefined protocols based on the performance

study either in an operating FC or in a liquid electrolyte electrochemical cell [15–20].

Again, from mechanism point of view, loss of electrochemical surface area (ECSA), a measure of catalytic activity of the catalyst, during such an AST may be categorized under several underlying mechanisms such as change of intrinsic catalyst activity (surface structure change), loss of catalyst loading due to dissolution, growth of particle size and electronic connectivity loss, as discussed in our previous study [21]. AST protocols meant to study the support corrosion use potentials (steady or dynamic) above 1.0 V vs. reversible hydrogen electrode (RHE) [22,23], where the Pt nanoparticles are passivated due to formation of Pt-oxide [24] layer and the activity loss may be attributed solely to the loss of electronic connectivity due to corrosion of carbon support to CO₂ (Eq. (1)) [25–28], leading to Pt nanoparticle detachment.



However, despite formation of passivation layer, owing to their high surface activity, nanoparticles of smaller diameter (~2 nm) may remain active through direct dissolution/redeposition of Pt at ~1.2 V [29], apart from carbon corrosion induced migration/agglomeration. Also, observational potential cycling (meant to observe activity loss) after a specified number of stress cycling (meant to support durability

* Corresponding author.

E-mail address: mashu@kbm.sdu.dk (S.M. Andersen).

<https://doi.org/10.1016/j.apcatb.2018.08.045>

Received 20 June 2018; Received in revised form 2 August 2018; Accepted 17 August 2018

Available online 23 August 2018

0926-3373/ © 2018 Elsevier B.V. All rights reserved.

study), which involves potentials as low as 0.0 V vs. RHE, remove the oxide layer formed during the stress cycling. Hence, frequent observational cycling may itself lead to significant degradation due to mechanisms other than support degradation. Indication of such degradation has been reported recently by using identical location transmission electron microscopy imaging, which suggest significant change of nanoparticle shape during potential cycling up to 1.3 V [30]. Again, Hitchcock have investigated the degradation mechanisms during different AST protocols using scanning tunneling X-ray microscopy [31]. However, the fractional contributions of different underlying mechanisms and the impact of observational cycles during AST on the ECSA loss has not been explored arguably.

The present study investigates the fractional contributions of different ECSA loss mechanisms during catalyst support oriented AST (potential cycling between 1.0 and 1.6 V) to provide fundamental knowledge for developing more realistic PEMFC catalyst screening protocols. The lower potential limit of 1.0 V is generally selected such that the Pt-oxide layer on Pt-nanoparticles remains intact and hence the activity loss takes place solely due to carbon corrosion. On the other hand, the upper limit of 1.6 V is selected to allow an accelerated carbon corrosion as significant carbon corrosion has been reported for potentials higher than 1.4 V [7–11,22]. However, potentials higher than 1.6 V are hardly used during PEMFC catalyst support corrosion AST protocols as oxygen evolution may affect the Pt/support interface adversely. The experiments were carried out in both 1 M H₂SO₄ of similar anion environment as PEMFCs (typically using perfluorinated sulfonic acid as electrode binder and electrolyte) and in 0.1 M HClO₄ of minimal anion adsorption as the most classical electrolyte for catalyst activity evaluations. The study also investigates the electrochemical behavior of the passivation layer during the AST cycling and impact of number of observational cycles.

2. Experimental methods

Catalyst ink, consisting of the 20 wt.% Pt supported on Vulcan XC-72 carbon Pt/C catalyst (BASF) and the ionomer (5 wt.% Nafion® solution, D521) in 85:15 solid weight ratio, was prepared through ultrasonic dispersion (2 min, ultrasonic probe; hielscher up200st) of catalyst and ionomer in isopropanol (IPA)/Milli-Q water mixture (2:1 v/v) to obtain a solid content of ~32 mg/ml. Working electrodes were prepared by drop-casting 5 µL of the ink on a polished (0.5 µm alumina) glassy carbon rotating disc electrode (GC RDE; 5 mm diameter, pine research instruments). X-ray fluorescence spectroscopy (XRF; Thermo Scientific Niton XL3t GOLDD + XRF analyzer) was employed to estimate the pre-AST and post-AST Pt-loadings on GC electrodes.

AST for support corrosion was performed both in 1 M H₂SO₄ and in 0.1 M HClO₄ electrolytes saturated with nitrogen (continuous bubbling) using a 3-electrode setup consisting of a graphitic carbon rod as the counter electrode (CE), a Hg/Hg₂SO₄ reference electrode (RE; REF 601 Radiometer®) and the catalyst ink coated GC RDE as working electrode (WE). All the potentials have been reported w.r.t. reversible hydrogen electrode (RHE). During AST, the WE was subjected to a linear sweep cyclic voltammetry (CV) cycling treatment (as per the protocol given in Table 1) using a Zahner®IM6e electrochemical workstation. In brief, the AST protocol consisted of stress cycling between 1.0 and 1.6 V for a total of 7500 cycles at a scan rate of 100 mV/s along with observation

cycling in between 0.02 and 1.2 V (scan rate 20 mV/s) for 2 cycles for ECSA evaluation after every 250 stress cycles. ECSA was estimated through measuring the charge/ g_{Pt} corresponding to H⁺ adsorption peak and using the surface charge density for H⁺ adsorption on polycrystalline Pt to be 210 (µC/cm). The starting and ending potentials (1.2 V) for the stress cycles as well as the observational cycles were selected to be marginally above the open circuit potential (OCV) of the working electrode in 1 M H₂SO₄ (OCV: ~1.1 V). Again, the observation cycles were started from the end potential of the stress cycles to avoid any removal/deposition of external species on the Pt-nanoparticles during switching between the stress and observational cycling.

In, while the change in Pt-loading due to dissolution was estimated through measurement of pre-AST and post-AST Pt-loadings using XRF, the change in average particle size of Pt-nanoparticles was estimated through X-ray diffraction (XRD) and transmission electron microscope (TEM) studies. The XRD patterns of pre-AST and post-AST samples were collected through a Rigaku Miniflex 600 X-ray diffractometer using Cu K α ($\lambda = 1.5418 \text{ \AA}$) radiation). TEM images were acquired using a JEOL JEM-2100 TEM operated at 100 kV.

3. Results and discussion

3.1. Typical degradation patterns

Durability study protocols using liquid electrolytes generally consider the ECSA and/or DLC variations with number of potential cycles (stress cycling) through observational CV (mostly in a potential range different from that of stress cycling) after certain number of stress cycles. The observational CV cycling is generally limited to a few (2–5) cycles and the stable CV after first cycle is used for the ECSA/DLC calculations while the first cycle is abandoned. However, as the first observational cycle after a specified number of stress cycles may contain significant information, we have analyzed both the observational cycles in this study.

Second cycle of the observational cyclic voltammograms of modified GC electrodes, recorded after each 250 potential cycles during the AST for 7500 cycles between 1.0 and 1.6 V in nitrogen saturated 1 M H₂SO₄ and 0.1 M HClO₄, have been shown in Fig. 1a and b, respectively. The voltammograms exhibit various characteristic peaks corresponding to reduction of Pt-oxides (0.8 V, cathodic scan), H⁺ adsorption (H_{upd}) peaks followed by a hydrogen evolution peak (between 0.3 and 0.02 V, cathodic scan), a hydrogen oxidation peak followed by H⁺ desorption (H stripping) peaks (between 0.02 and 0.3 V, anodic scan) and Pt-oxide formation peaks (between 0.8 and 1.2 V, anodic scan). Apart from this, a double layer region between 0.6 and 0.4 V characterized by the absence of any Faradaic peaks, can also be observed in the voltammograms. Further, the broad anodic peak between 0.6 and 0.7 V, may be attributed to oxidation of hydroquinone generated from carbon corrosion during stress cycling to quinone [32]. Absence of this peak in the initial voltammogram (0 stress cycle) confirms its origin to be the carbon corrosion during AST.

The high fractional loss of ECSA (~50% in 0.1 M HClO₄ and ~55% in 1 M H₂SO₄) during AST for 7500 cycles at a scan rate of 100 mV/s between 1.0 and 1.6 V may be compared with previous reports. For example, Riese et al. have reported ~30% ECSA loss during AST for 5000 cycles at a scan rate of 500 mV/s between 1.0 and 1.5 V in 0.09 M H₂SO₄ [22]. The lower ECSA loss may be attributed to the higher scan rate, leading to lower particle growth [33]. The ECSA loss of the present study may also be compared with that by Joen et al., suggesting ~70% ECSA loss during AST of Pt/C (40 wt.% Pt) for 6000 cycles at a scan rate of 100 mV/s between 1.0 and 1.6 V in 0.5 M H₂SO₄ [34].

Further, the variations of ECSA with potential cycles in 1 M H₂SO₄ and 0.1 M HClO₄, measured through integrating the area of H⁺ desorption peaks below the double layer current have been shown in Fig. 1c. On the other hand, corresponding variations of DLC with potential cycling, estimated through cathodic and anodic currents at 0.4 V, have

Table 1
AST protocol for support corrosion study.

Cycling type	Potential (V)				Scan rate (mV/s)
	start	upper	lower	end	
Stress	1.2	1.6	1.0	1.2	100
Observational	1.2	1.2	0.02	1.2	20

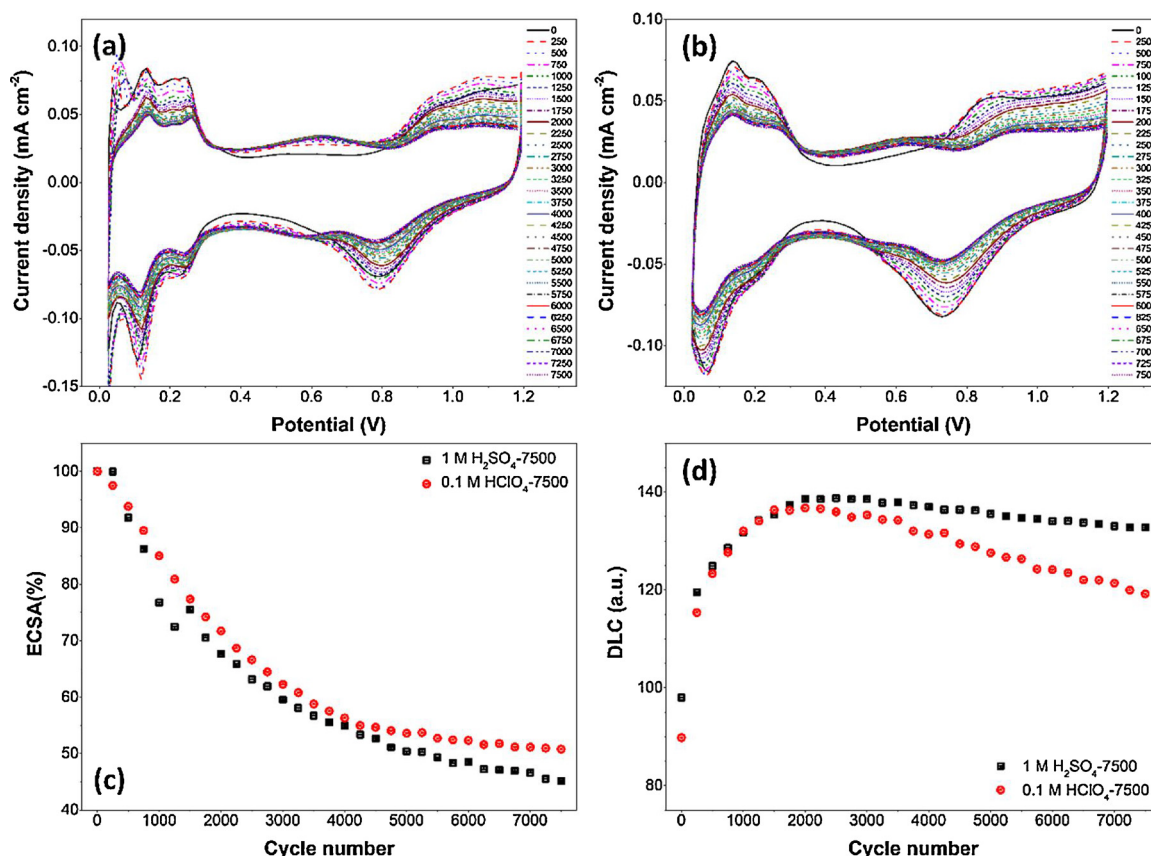


Fig. 1. Cyclic voltammograms (second cycle) of GC modified with catalyst ink (Pt/C) in nitrogen saturated (a) 1 M H₂SO₄ and (b) 0.1 M HClO₄ electrolytes, recorded after each 250 potential cycles of the AST for support corrosion study. Corresponding variations of (c) ECSA and (d) DLC with stress cycle number.

been depicted in Fig. 1d. It is evident that unlike ECSA, which decreases monotonously with potential cycling, the DLC shows a more complex variation with a sharp initial increase with potential cycling to reach a maximum for ~2000 cycles followed by a gradual decrease. The initial increase of DLC may be attributed to initial increase of hydrophilicity due to formation of oxide functional groups [35,36] on the carbon surface during potential cycling, leading to increased accessible area for charge transfer. Further, dominance of the differential surface area loss due to carbon corrosion over the differential increment of wetting, possibly due to saturation of functional group density, leads to gradual decrease of DLC for potential cycles higher than 2000. Furthermore, for potential cycles higher than 2000, the DLC decreases with a faster rate in 0.1 M HClO₄ as compared to that in 1 M H₂SO₄. This may be attributed to strong adsorption of bisulfate and/or oxide functional groups on carbon surface in 1 M H₂SO₄, leading to decreased surface activity and hence, less corrosion. Hence, unlike for the potential window between 0.4 and 1.6 V of our previous study [21], a one-to-one correspondence between ECSA loss due to carbon corrosion and DLC variations cannot be established for the potential cycling between 1.0 and 1.6 V potential window.

3.2. Adsorption species studies

First cycle of the observational cyclic voltammograms of modified GC electrodes, recorded after each 250 potential cycles during the AST in nitrogen saturated 1 M H₂SO₄ and 0.1 M HClO₄, have been shown in Fig. 2a and b, respectively. The most significant information contained in this cycle may be correlated to the nature of the passivation layer, i.e., the adsorbed species on Pt nanoparticles during stress cycling. As

can be observed from Fig. 2a and b, the first observation cycle at the beginning of AST (0 stress cycles), which has been recorded just after activation of the electrode, exhibits a cathodic peak corresponding to Pt-oxide reduction reaction, centered at ~800 mV and much similar to that observed in the second observational cycle (Fig. 1a and b). On the other hand, the first observational cycle after certain number of stress cycling exhibits a more intense peak, probably corresponding the reduction of the Pt-oxide passivation layer formed during stress cycling. As can be seen clearly from Fig. 2a and b, the potential corresponding to the said reduction peak varies significantly with number of stress cycles. Variations of the potential corresponding to this peak for AST in 1 M H₂SO₄ and 0.1 M HClO₄ electrolytes have been shown in Fig. 2c and d, respectively. The observed peak potential variations suggest significant change in the nature of surface adsorbed species with the increasing number of stress cycles. More negative reduction potentials corresponding to higher number of stress cycles signify stronger adsorption/different adsorbed species obtained possibly from carbon corrosion. Although the altered crystallite size and surface structure (crystalline facets) during AST may also cause minor shift of the adsorption peak, the large shifts (> 200 mV) may not be accounted for such an origin.

Similar position and evolution of adsorption peaks were observed for the studies with both sulfuric and perchloric acid as electrolyte, though sulfonic group is documented stronger adsorbing anion on Pt surface than perchloric. This may indicate that the electrolyte anions does not play a significant role in the adoption process in comparison to degenerated carbon species from carbon corrosion. This may also imply that oxidized carbon species may strongly adsorb on Pt catalyst surface and influence the performance of PEMFCs.

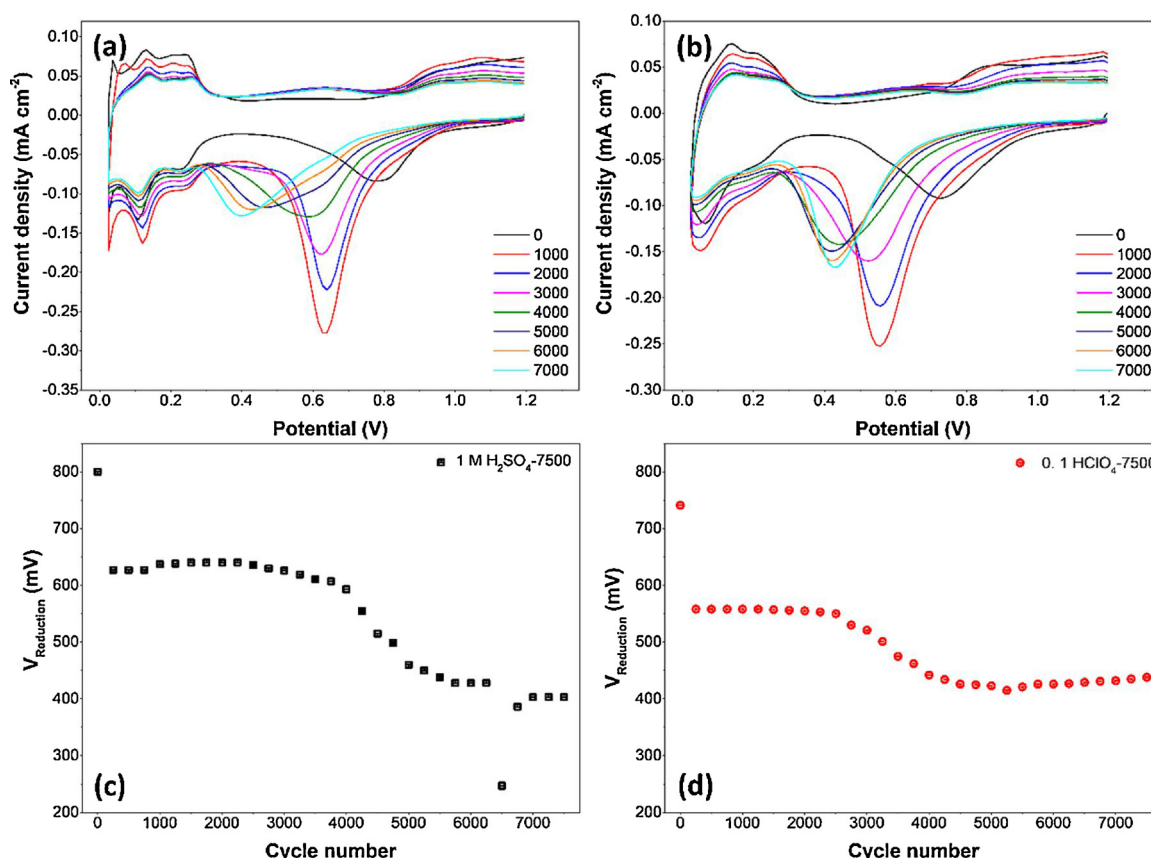


Fig. 2. Cyclic voltammograms (first cycle) of GC modified with catalyst ink (Pt/C) in nitrogen saturated (a) 1 M H₂SO₄ and (b) 0.1 M HClO₄ electrolytes, recorded after each 250 potential cycles between 1.0 and 1.6 V (100 mV/s). Variations of the potential corresponding to Pt-oxide reduction/desorption peak with stress cycle number for (c) 1 M H₂SO₄ and (d) 0.1 M HClO₄ electrolytes.

3.3. Effect of observational cycles on durability

Observational cycles in a potential window corresponding to various redox reactions on the Pt surface may itself cause significant ECSA loss during the AST meant for support durability study. This may lead to significant ECSA loss to provide misleading results in some cases. In an attempt to estimate such ECSA loss quantitatively, AST in 1 M H₂SO₄ has been carried out by reducing the number of stress cycles between two observational CV cycles from 250 to 1 cycle while keeping the number of observational cycles to be the same as that of the AST for support corrosion (2 cycles in each observational CV measurement; total 31 measurements). The single stress cycle (1.0–1.6 V) between two observational CV measurements is used to form the passivation layer on catalyst particles, which is removed during the first observational cycle. The second and first observational cycles from each observational measurement (0–30 stress cycles) have been shown in Fig. 3a and b, respectively. The evolution of CV plots of Fig. 3a with stress cycles suggests negligible support corrosion with marginal change of DLC (Fig. 3c; initial increase followed by saturation) and a very weak peak corresponding to oxidation of hydroquinone. However, the ECSA changes significantly, with > 25% loss of ECSA (Fig. 3c). Again, the first cycle of the observational CV measurements exhibits the Pt-oxide reduction peak at a comparatively constant potential value for different measurement cycles (Fig. 3d), suggesting no significant carbon corrosion responsible for the generation of species having more negative reduction potentials. Hence, the number of observational cycles in an AST protocol meant otherwise for the carbon support corrosion affects the catalyst activity and ECSA significantly.

3.4. ECSA loss due to particle growth

Platinum surface is considered to be unaffected due to formation of Pt-oxide layer when kept at a potential value higher than its standard oxidation potential. Hence, under potential cycling between 1.0 and 1.6 V, the catalyst layer activity loss is attributed mainly to the degradation of the catalyst support. However, growth of the Pt nanoparticles through Ostwald ripening cannot be discarded due to limited (however small) solubility of the Pt-oxide species [37] in aqueous solutions. Again, other mechanisms such as particle coalescence, agglomeration, etc. may be present due to corrosion of the support. The small solubility of the Pt-oxide species, combined with Pt²⁺ reduction of Pt below ~1.2 V [29] during potential cycling, may cause considerable change in the particle size through Ostwald ripening process over prolonged time scales that are typically used in AST protocols for support corrosion (for example, 7500 potential cycles between 1.0 and 1.6 V at a scan rate of 100 mV/s take ~25 h). Hence, ECSA loss due to Pt nanoparticle coarsening may contribute significantly to the total ECSA loss during an AST meant to study the support corrosion.

Such a coarsening of the Pt nanoparticles has been studied through XRD patterns of pristine and post-AST samples. As shown in Fig. 4, the XRD patterns exhibit diffraction peaks corresponding to Pt (111) and Pt (200) planes at 2θ values of 39.8° and 46.1° (JCPDS# 65-2868), respectively [38]. The width (FWHM) of the Pt (111) peak, obtained by fitting the data using Gaussian distributions, has been used to estimate the average crystallite size (L) of the Pt-nanoparticles on an electrode through Scherrer formula ($L = 0.9\lambda/\beta\cos\theta$; where λ , θ and β are the X-ray wavelength, the diffraction angle and the FWHM ($2\Delta\theta$),

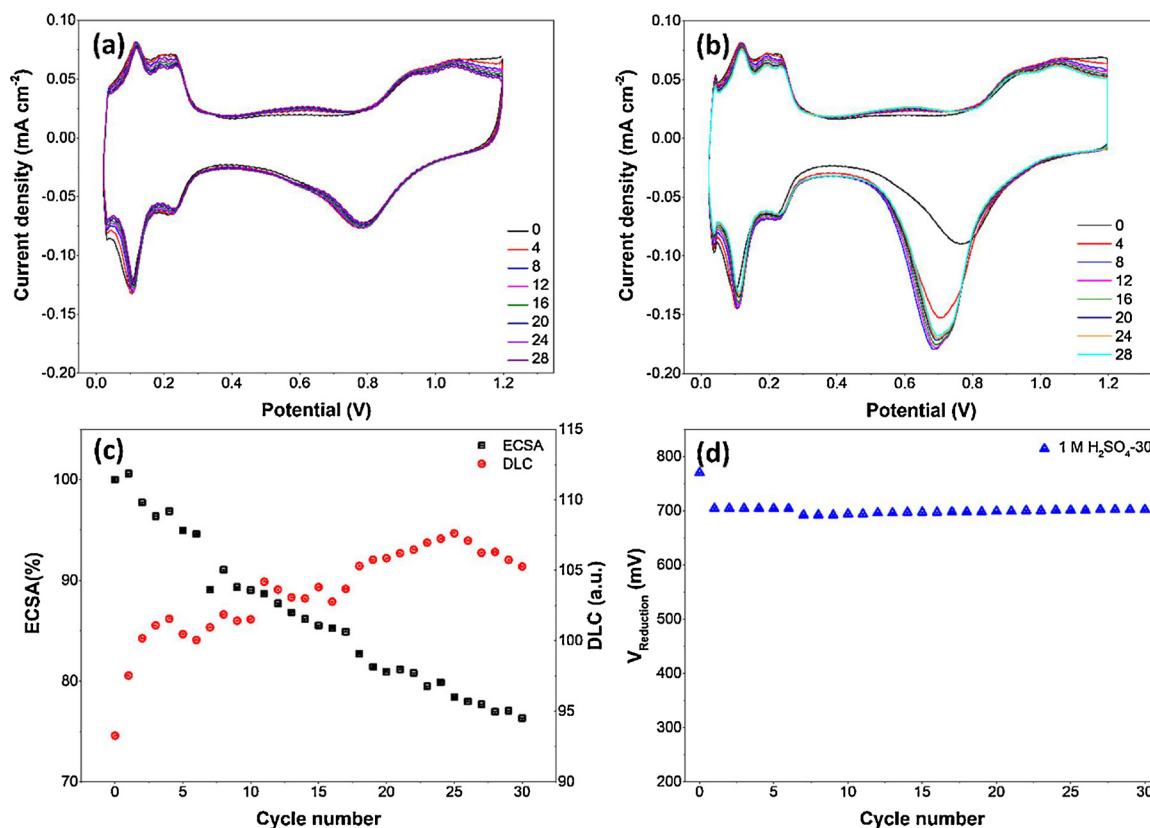


Fig. 3. Cyclic voltammograms (a) second cycle and (b) first cycle of observational CV measurements on a GC electrode modified with catalyst ink (Pt/C) in nitrogen saturated 1 M H₂SO₄ electrolyte, recorded after each 1 potential cycle between 1.0 and 1.6 V (100 mV/s). (c) Corresponding variations of ECSA and DLC with stress cycle number. (d) Variations of the potential corresponding to Pt-oxide reduction/desorption peak with stress cycle number.

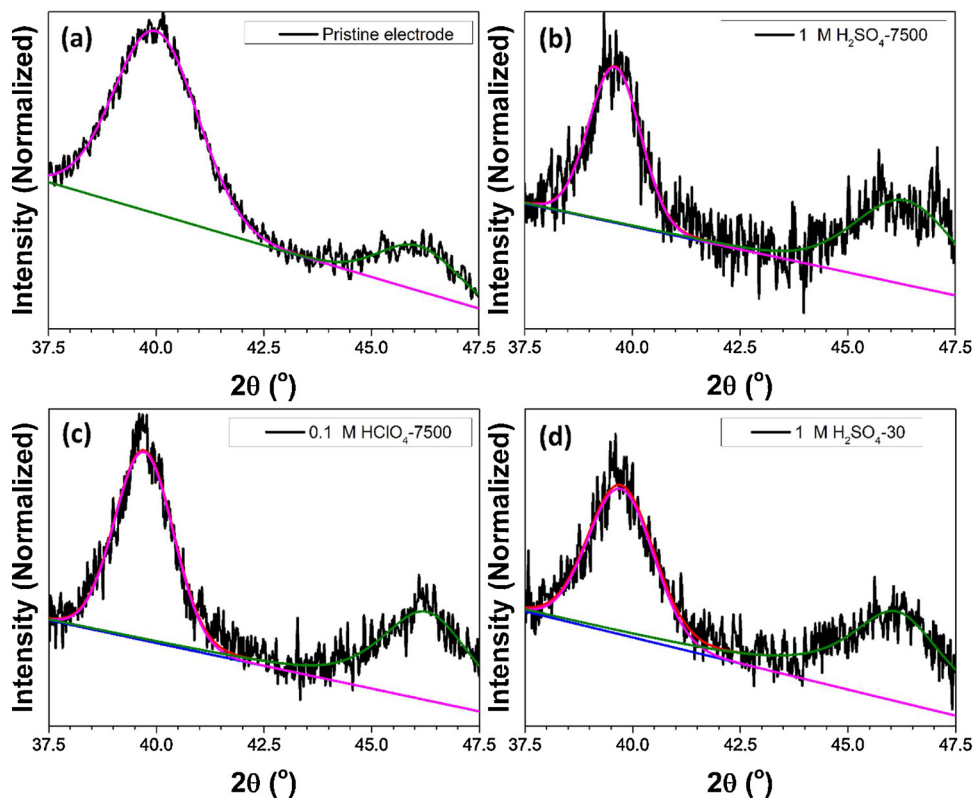


Fig. 4. XRD patterns showing Pt (111) and Pt (200) peaks respectively at ~40° and ~46° for (a) Pristine (pre-AST), (b) post-AST ink (7500 potential cycles in 1 M H₂SO₄), (c) post-AST ink (7500 potential cycles in 0.1 M ClO₄) and (d) post-AST ink (30 potential cycles in 1 M H₂SO₄). Smooth lines represent the fitted curves using Gaussian distributions above the linear background.

Table 2
Average crystallite sizes for various electrodes estimated from XRD.

Sample description	FWHM	Crystalline size (nm)	% Growth
Pristine catalyst ink	2.56	3.3	–
30 AST cycles in 1 M H ₂ SO ₄	1.88	4.5	36
7500 AST cycles in 1 M H ₂ SO ₄	1.42	6.0	80
7500 AST cycles in 0.1 M HClO ₄	1.63	5.2	57

respectively). As compared to that of pristine sample (Fig. 4a), the XRD patterns of post-AST samples (Fig. 4b–d) exhibit reduced width of Pt (111) diffraction peak, and hence, significant growth of the crystallites during AST, as shown in Table 2. The average crystallite size values for various samples may be overestimated due to the uncorrected instrumental broadening of the peaks. However, this does not hinder a relative comparison, suggesting significant coarsening of the Pt-nanoparticles and hence, reduction of surface area during the AST for support corrosion.

The growth of catalyst particles during AST has also been confirmed through TEM imaging of the pristine and the post-AST samples shown in Fig. 5. The corresponding distributions of particle sizes, estimated using ImageJ software through measuring the area of closest ellipse fit to the visible Pt-nanoparticles in the TEM image while excluding the obvious agglomerates have been shown as insets in Fig. 5a and b. As can be observed in Fig. 5, the average particle size of the Pt nanoparticles increases significantly from 2.6 nm to 3.9 nm during AST in 1 M H₂SO₄ for 7500 potential cycles (1.0–1.6 V; 100 mV/s).

3.5. Quantification of ECSA loss pathways

Owing to the observed growth of Pt nanoparticles, the ECSA loss during AST cannot be assigned completely to the degradation of support. Possible mechanisms to the ECSA loss may include (i) the loss of electronic connectivity of the catalyst particles (l_e), (ii) the loss of catalyst loading due to dissolution (l_d) and (iii) the loss due to growth of particles (l_a). The fractional contributions of said degradation mechanisms has been calculated using the following relationship (Eq. (2)).

$$\frac{ECSA_f}{ECSA_i} = \left[1 - (l_d + l_e + l_{H^+}) \right] \times \frac{R_i}{R_f} \quad (2)$$

where, $ECSA_i$, $ECSA_f$, are the initial and final ECSA, R_i and R_f are the initial and final particle sizes, respectively, and l_{H^+} is the loss contribution due to proton connectivity loss (ionomer degradation) with the last being zero ($l_{H^+} = 0$) for AST in liquid electrolytes. R_i and R_f estimated from XRD have been used for the quantification calculations as the TEM particle size estimation uses a relatively smaller number of particles from the image, while all the crystallites from the sample contribute the XRD pattern.

While l_d is obtained directly from the initial and final loadings of Pt on the electrode, l_e and l_a are estimated using Eqs. (3) and (4), respectively (detailed mathematical derivation of Eqs. (2)–(4): supporting information S1).

$$l_e = 1 - l_d - \left(\frac{ECSA_f}{ECSA_i} \times \frac{R_i}{R_f} \right) \quad (3)$$

$$l_a = (1 - (l_d + l_e)) \times \left(1 - \frac{R_i}{R_f} \right) \quad (4)$$

Here, the loss of DLC has not been used to determine l_e as the change in DLC is affected by several factors such as (i) increased wettability by change of surface chemistry, (ii) increased surface area by change of microstructure, (iii) decreased surface area due to electrochemical degradation (oxidation) of the carbon support, etc., leading to its variation with stress cycle number to pass through a maximum.

Fractional contributions of different degradation mechanisms have been shown in Fig. 6 for all the 3 AST conditions (electrolyte/stress cycle variations). It can be seen clearly from Fig. 6 that the AST protocol used for support corrosion study has a significant effect on the catalyst particles. Apart from loss of electronic connectivity, ~50% of ECSA loss may be assigned to the growth of catalyst crystallites.

Significant contribution due to crystalline size growth during AST protocol suggests pronounced effect of initial size (particle/crystalline) distribution on the ECSA loss during AST. As catalysts with smaller initial size may be more active towards dissolution/redeposition growth, the support durability should be compared using similar size distributions of the catalyst particles. Moreover, for support focused AST protocols,

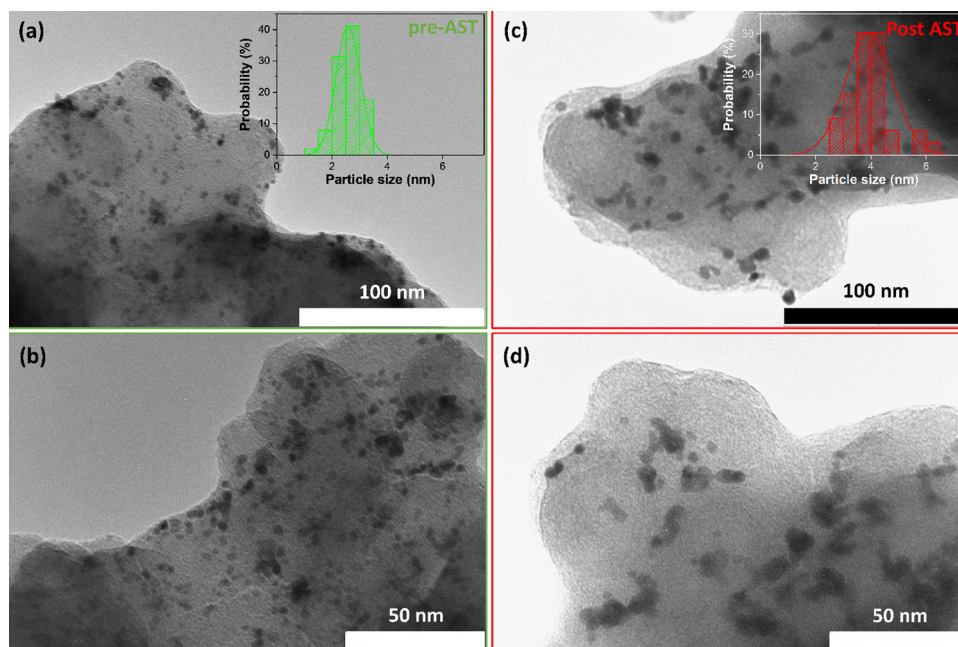


Fig. 5. TEM images of Pt/C catalyst (20 wt.% Pt on carbon) before (a–b) and after (c–d) AST in 1 M H₂SO₄ for 7500 potential cycles (1.0–1.6 V; 100 mV/s). Corresponding particle size distribution histograms have been shown as inset of (a) and (c).

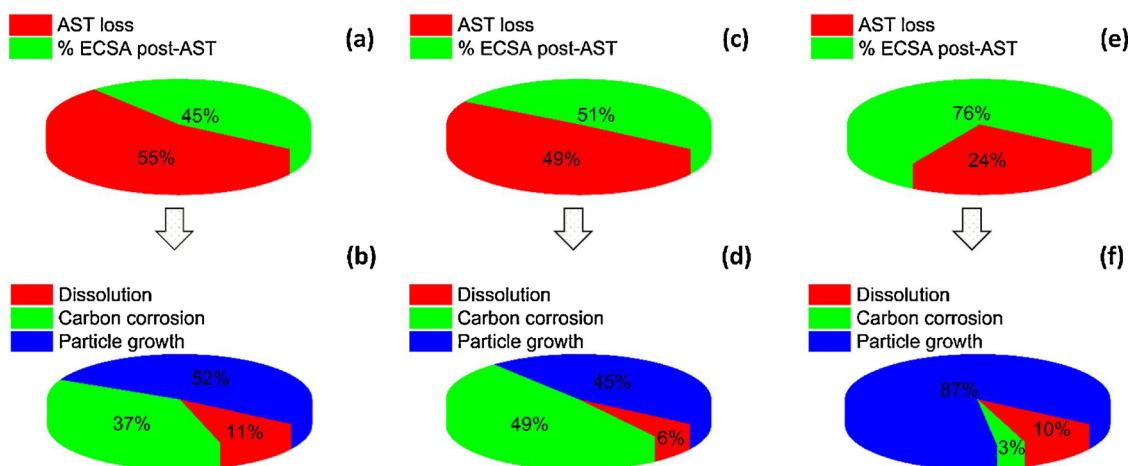


Fig. 6. Variations of ECSA loss % (a, c and e) for different AST conditions and corresponding fractional contributions of different ECSA loss mechanisms (b, d and f). (a) and (b) AST (7500 cycles) in 1 M H₂SO₄, (c) and (d) AST (7500 cycles) in 0.1 M HClO₄ and (e) and (f) AST (30 cycles) in 1 M H₂SO₄.

observational cycles, involving potential lower than platinum deposition potential ($\text{PtO}_2 + 4\text{H}^+ + 4\text{e}^- \leftrightarrow \text{Pt} + 2\text{H}_2\text{O}$; 1.00 V vs. RHE), should be avoided to minimize redeposition of soluble platinum species related particle growth. Moreover, as the Pt dissolution rate depends significantly on scan rate with higher dissolution at slower scan rates [33], the fractional loss associated to particle growth is expected to increase for AST protocols using slower scan rates (e.g. 50 mV/s).

4. Conclusion

In conclusion, AST protocol for support corrosion has been investigated for the fractional contributions of possible ECSA loss mechanisms, namely electronic connectivity loss, dissolution loss and particle growth loss. The study suggests ~50% loss due to particle growth, which may depend on factors other than the durability of the support (e.g. initial average size of the catalyst and frequency of redeposition). Hence, such a fractional quantification may be used to estimate the support durability more effectively by eliminating the effect of ECSA loss variation due to factors not related to support degradation.

Acknowledgements

The authors appreciate Prof. Niels Marcussen, Bioanalytic Karin Trampedach and Aleksandra Maria Rojek for their assistance in TEM. The authors appreciate the financial support from VILLUM FONDEN blokstipendier, UpCat (ForskEL J.No 2015-1-12315), and from the Danish Council for Strategic Research, Innovation Fond Denmark, through the 4M Centre (J.No 12-132710).

Appendix A. Supplementary data

Supplementary material related to this article can be found, in the online version, at doi:<https://doi.org/10.1016/j.apcatb.2018.08.045>.

References

- [1] J. Zhang, PEM Fuel Cell Electrocatalysts and Catalyst Layers: Fundamentals and Applications, Springer Science & Business Media, London, 2008.
- [2] J. Gong, K. Sumathy, Q. Qiao, Z. Zhou, Review on dye-sensitized solar cells (DSSCs): advanced techniques and research trends, *Renew. Sustain. Energy Rev.* 68 (2017) 234–246.
- [3] J. Wu, X.Z. Yuan, J.J. Martin, H. Wang, J. Zhang, J. Shen, S. Wu, W. Merida, A review of PEM fuel cell durability: degradation mechanisms and mitigation strategies, *J. Power Sources* 184 (2008) 104–119.
- [4] L. Dubau, L. Castanheira, F. Maillard, M. Chatenet, O. Lottin, G. Maranzana, J. Dillet, A. Lamibrac, J.C. Perrin, E. Moukheiber, A. Elkaddouri, G.D. Moor, C. Bas, L. Flandin, N. Caqué, A review of PEM fuel cell durability: materials degradation,

- local heterogeneities of aging and possible mitigation strategies, *Wiley Interdiscip. Rev. Energy Environ.* 3 (2014) 540–560.
- [5] S. Zhang, X.-Z. Yuan, J.N.C. Hin, H. Wang, K.A. Friedrich, M. Schulze, A review of platinum-based catalyst layer degradation in proton exchange membrane fuel cells, *J. Power Sources* 194 (2009) 588–600.
- [6] Y. Yu, H. Li, H. Wang, X.-Z. Yuan, G. Wang, M. Pan, A review on performance degradation of proton exchange membrane fuel cells during startup and shutdown processes: causes, consequences, and mitigation strategies, *J. Power Sources* 205 (2012) 10–23.
- [7] J. Kim, J. Lee, Y. Tak, Relationship between carbon corrosion and positive electrode potential in a proton-exchange membrane fuel cell during start/stop operation, *J. Power Sources* 192 (2009) 674–678.
- [8] P. Ferreira-Aparicio, A.M. Chaparro, M.A. Folgado, J.J. Conde, E. Brightman, G. Hinds, Degradation study by start-up/shut-down cycling of superhydrophobic electrosprayed catalyst layers using a localized reference electrode technique, *ACS Appl. Mater. Interfaces* 9 (2017) 10626–10636.
- [9] Q. Shen, M. Hou, D. Liang, Z. Zhou, X. Li, Z. Shao, B. Yi, Study on the processes of start-up and shutdown in proton exchange membrane fuel cells, *J. Power Sources* 189 (2009) 1114–1119.
- [10] W.R. Baumgartner, P. Parz, S.D. Fraser, E. Wallnöfer, V. Hacker, Polarization study of a PEMFC with four reference electrodes at hydrogen starvation conditions, *J. Power Sources* 182 (2008) 413–421.
- [11] H. Tang, Z. Qi, M. Ramani, J.F. Elter, PEM fuel cell cathode carbon corrosion due to the formation of air/fuel boundary at the anode, *J. Power Sources* 158 (2006) 1306–1312.
- [12] Y.-J. Wang, D.P. Wilkinson, J. Zhang, Noncarbon support materials for polymer electrolyte membrane fuel cell electrocatalysts, *Chem. Rev.* 111 (2011) 7625–7651.
- [13] L. Du, Y. Shao, J. Sun, G. Yin, J. Liu, Y. Wang, Advanced catalyst supports for PEM fuel cell cathodes, *Nano Energy* 29 (2016) 314–322.
- [14] E. Antolini, Carbon supports for low-temperature fuel cell catalysts, *Appl. Catal. B* 88 (2009) 1–24.
- [15] N. Garland, T. Benjamin, J. Kopasz, DOE fuel cell program: durability technical targets and testing protocols, *ECS Trans.* 11 (2007) 923–931.
- [16] A.A. Franco, M. Gerard, M. Guinard, B. Barthe, O. Lemaire, Carbon catalyst-support corrosion in polymer electrolyte fuel cells: mechanistic insights, *ECS Trans.* 13 (2008) 35–55.
- [17] S.M. Andersen, L. Grahl-Madsen, Interface contribution to the electrode performance of proton exchange membrane fuel cells – impact of the ionomer, *Int. J. Hydrogen Energy* 41 (2016) 1892–1901.
- [18] S.M. Andersen, E. Skou, Electrochemical performance and durability of carbon supported Pt catalyst in contact with aqueous and polymeric proton conductors, *ACS Appl. Mater. Interfaces* 6 (2014) 16565–16576.
- [19] S. Ye, M. Hall, P. He, PEM fuel cell catalysts: the importance of catalyst support, *ECS Trans.* 16 (2008) 2101–2113.
- [20] R. Mukundan, G. James, D. Ayotte, J.R. Davey, D. Langlois, D. Spornjak, D. Torracco, S. Balasubramanian, A.Z. Weber, K.L. More, R.L. Borup, Accelerated testing of carbon corrosion and membrane degradation in PEM fuel cells, *ECS Trans.* 50 (2013) 1003–1010.
- [21] R. Sharma, S.M. Andersen, Quantification on degradation mechanisms of polymer electrolyte membrane fuel cell catalyst layers during an accelerated stress test, *ACS Catal.* 8 (2018) 3424–3434.
- [22] A. Riese, D. Banham, S. Ye, X. Sun, Accelerated stress testing by rotating disk electrode for carbon corrosion in fuel cell catalyst supports, *J. Electrochem. Soc.* 162 (2015) F783–F788.
- [23] S. Park, Y. Shao, V.V. Viswanathan, J. Liu, Y. Wang, Non-kinetic losses caused by electrochemical carbon corrosion in PEM fuel cells, *Int. J. Hydrogen Energy* 37 (2012) 8451–8458.
- [24] S.R. Dhanushkodi, M. Tam, S. Kundu, M.W. Fowler, M.D. Pritzker, Carbon corrosion fingerprint development and de-convolution of performance loss according to

- degradation mechanism in PEM fuel cells, *J. Power Sources* 240 (2013) 114–121.
- [25] L. Castanheira, W.O. Silva, F.H.B. Lima, A. Crisci, L. Dubau, F. Maillard, Carbon corrosion in proton-exchange membrane fuel cells: effect of the carbon structure, the degradation protocol, and the gas atmosphere, *ACS Catal.* 5 (2015) 2184–2194.
- [26] F. Forouzandeh, X. Li, D.W. Banham, F. Feng, S. Ye, V. Birss, Evaluation of the corrosion resistance of carbons for use as PEM fuel cell cathode supports, *J. Electrochem. Soc.* 162 (2015) F1333–F1341.
- [27] L.M. Roen, C.H. Paik, T.D. Jarvi, Electrocatalytic corrosion of carbon support in PEMFC cathodes, *Electrochem. Solid-State Lett.* 7 (2004) A19–A22.
- [28] H. Schulenburg, B. Schwanitz, N. Linse, G.G. Scherer, A. Wokaun, J. Krbanjevic, R. Grothausmann, I. Manke, 3D imaging of catalyst support corrosion in polymer electrolyte fuel cells, *J. Phys. Chem. C* 115 (2011) 14236–14243.
- [29] L. Tang, X. Li, R.C. Cammarata, C. Friesen, K. Sieradzki, Electrochemical stability of elemental metal nanoparticles, *J. Am. Chem. Soc.* 132 (2010) 11722–11726.
- [30] R.M. Arán-Ais, Y. Yu, R. Hovden, J. Solla-Gullón, E. Herrero, J.M. Feliu, H.D. Abruña, Identical location transmission electron microscopy imaging of site-selective Pt nanocatalysts: electrochemical activation and surface disordering, *J. Am. Chem. Soc.* 137 (2015) 14992–14998.
- [31] A.P. Hitchcock, V. Berejnov, V. Lee, M. West, V. Colbow, M. Dutta, S. Wessel, Carbon corrosion of proton exchange membrane fuel cell catalyst layers studied by scanning transmission X-ray microscopy, *J. Power Sources* 266 (2014) 66–78.
- [32] D. Schonvogel, J. Hülstede, P. Wagner, I. Kruusenberg, K. Tammeveski, A. Dyck, C. Agert, M. Wark, Stability of Pt nanoparticles on alternative carbon supports for oxygen reduction reaction, *J. Electrochem. Soc.* 164 (2017) F995–F1004.
- [33] A.A. Topalov, I. Katsounaros, M. Auinger, S. Cherevko, J.C. Meier, S.O. Klemm, K.J.J. Mayrhofer, Dissolution of platinum: limits for the deployment of electrochemical energy conversion? *Angew. Chem. Int. Ed.* 51 (2012) 12613–12615.
- [34] Y. Jeon, Y. Ji, Y.I. Cho, C. Lee, D.-H. Park, Y.-G. Shul, Oxide–carbon nanofibrous composite support for a highly active and stable polymer electrolyte membrane fuel-cell catalyst, *ACS Nano* 12 (2018) 6819–6829.
- [35] H.-S. Oh, K. Kim, Y.-J. Ko, H. Kim, Effect of chemical oxidation of CNFs on the electrochemical carbon corrosion in polymer electrolyte membrane fuel cells, *Int. J. Hydrogen Energy* 35 (2010) 701–708.
- [36] S. Hu, P. Bai, F. Tian, S. Cao, J. Sun, Hydrophilic carbon onions synthesized by millisecond pulsed laser irradiation, *Carbon* 47 (2009) 876–883.
- [37] P.J. Ferreira, G.J. la O', Y. Shao-Horn, D. Morgan, R. Makharia, S. Kocha, H.A. Gasteiger, Instability of Pt / C electrocatalysts in proton exchange membrane fuel cells: a mechanistic investigation, *J. Electrochem. Soc.* 152 (2005) A2256–A2271.
- [38] X.-C. Liu, G.-C. Wang, R.-P. Liang, L. Shi, J.-D. Qiu, Environment-friendly facile synthesis of Pt nanoparticles supported on polydopamine modified carbon materials, *J. Mater. Chem. A* 1 (2013) 3945–3953.